Vibration Isolation for Cavity Quantum Electrodynamics

Thesis by

Stephen Travis Bannerman

In Partial Fulfillment of the Requirements

for the Degree of

Bachelor of Science

California Institute of Technology

Pasadena, California

2006

(Submitted May 1, 2006)

Acknowledgements

First of all I would like to thank Jeff Kimble for giving me the opportunity to see what cavity QED and quantum optics are all about. I am grateful to Tracy Northup for spending so much time helping me get my feet wet in experimental physics, especially during my first year working in the group. Additionally, I am greatly indebted to Dalziel Wilson for his ideas and help throughout the year. I would also like to thank Yat Shan Au and Andrey Rodionov for their help. I would like to thank Riccardo De Salvo, without whom none of the mini-GAS work would have been possible. Finally, I am most indebted to my family who has supported me throughout my time at Caltech.

Abstract

The mechanical stability of an optical resonator in cavity quantum electrodynamics experiments is crucial to establishing and maintaining strong coupling between an atom and the electromagnetic field of a photon. Vibrational noise from seismic and acoustic sources inside the laboratory is the largest impediment to the resonator's stability, and it is thus necessary to deliberately isolate the cavity from vibration. Efforts have been underway to create a new cavity QED experiment in the Kimble Group, with a major goal being to lower the background pressure in the cavity's vacuum chamber by an order of magnitude. This requires the design of a new vibration isolation system, comprising low outgassing elements bakeable to high temperatures. This thesis describes two new designs for vibration isolation which meet these requirements. One design, which employs blade springs similar to those found in gravitational wave interferometers, regrettably could not completed in the timeframe of this thesis. The other design utilizes a perfluoroelastomer as its elastic element. It was tested and shown perform as effectively as the previous vibration isolation system.

Contents

Chapter 1

Background

This chapter is intended to provide general context for this thesis. Section 1.1 discusses the basic theory behind cavity quantum electrodynamics as well as some of the experiments which have taken place in the Kimble group. Section 1.2 discusses the experimental motivation and goals for building a new experiment, including the requirements imposed by these goals for developing a new vibration isolation system. Finally, Section 1.3 covers the basics of vibration isolation and introduces several common vibration isolation techniques.

1.1 Cavity Quantum Electrodynamics

The field of quantum control and measurement has been a fascinating direction of research in modern physics, with promising applications to the emerging field of quantum information science [1]. Over the last decade, many research groups have been focusing their attention on the development of the tools to study dynamical processes of individual quantum systems. Research in this field takes many forms, including Coulomb blockades with discrete electronic energy spectra [2], trapped and cooled ions [3], and cavity quantum electrodynamics (QED) [4].

The Quantum Optics Group at Caltech has undertaken the latter area of research. In particular, we study cavity QED in the regime of strong coupling, wherein the dissipative energy loss rates of the atom-cavity system are much smalller than the rates of energy exchange within the system.

1.1.1 Theory

Cavity QED experiments probe the electric-dipole interactions between photons and atoms. The dynamics of single atoms and photons can be studied by employing high quality optical cavities. The Kimble group employs a traditional Fabry-Perot resonator comprising two spherical mirrors with highly reflective coatings separated at some distance l. We can characterize the cavity by its finesse ($\mathcal{F}$) which is given by

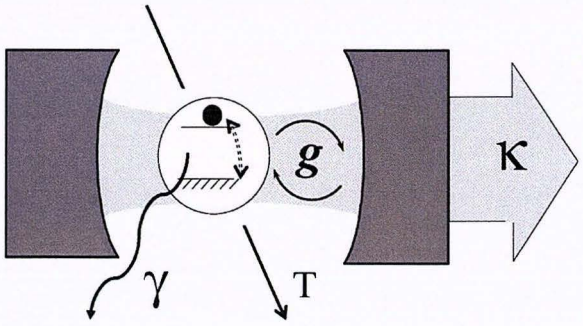

Figure 1.1: Schematic of a Fabry-Perot cavity with characterstic rates shown: κ is the cavity decay rate, γ is the rate of spontaneous atomic decay, T is the atom transit time through the cavity mode, and g is the rate of coherent atom-field coupling. Strong coupling is achieved when $g \gg (\kappa, \gamma, T^{-1})$ [5].

$$\mathcal{F} = \frac{\pi}{T + A} = \frac{\Delta\nu_{fsr}}{2\kappa} \tag{1.1}$$

where T is the transmission power coefficient for each mirror, A is the absorption/scattering power coefficient for each mirror, $\Delta\nu_{fsr} = \frac{c}{2l}$ is the frequency span between longitudinal modes of the cavity (free spectral range), and 2κ is the linewidth of the cavity (full width at half max).

Figure 1.1 shows a schematic of a Fabry-Perot cavity with a two level atom coupled to the cavity mode. This coupling is due to the interaction between the electric dipole of the atom and the electromagnetic field inside the cavity. An ideal atom-cavity system with no dissipation can be described by the Jaynes-Cummings Hamiltonian [6],

$$H = \hbar\omega a^\dagger a + \hbar\omega\frac{\sigma_z}{2} + \hbar g_0(a^\dagger\sigma_- + \sigma_+ a) \tag{1.2}$$

where ω is the resonant frequency of both the atom and cavity, $(a, a^\dagger)$ are the field annihilation and creation operators, and (σ_-, σ_+) are the atomic lowering and raising operators. Diagonalizing this Hamiltonian at n system excitations yields the Jaynes-Cummings ladder of eigenstates

$$|\pm\rangle_n = \frac{1}{\sqrt{2}}(|g, n\rangle \pm |e, n-1\rangle \tag{1.3}$$

with energy eigenvalues

$$E_{\pm n} = n\hbar\omega \pm \sqrt{n}\hbar g_0 \tag{1.4}$$

as illustrated in Figure 1.2.

These atom-cavity eigenstates can be observed through the vacuum-Rabi splitting (see Figure 1.3), which is the hallmark of strong coupling. When an atom becomes coupled with the electromagnetic field of a cavity, the transmission spectrum of the cavity splits from

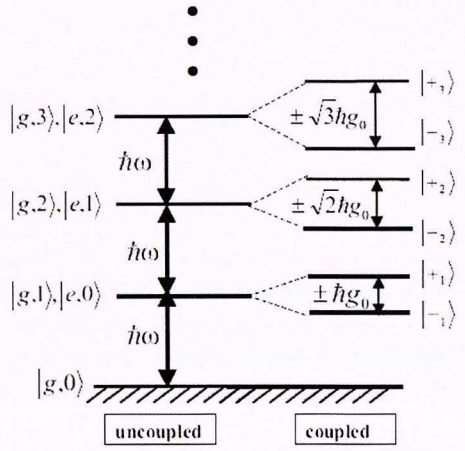

Figure 1.2: The Jaynes-Cummings ladder of eigenstates: $|(g,e),n\rangle$ corresponds to the atomic (ground, excited) state with n quanta of excitation [7].

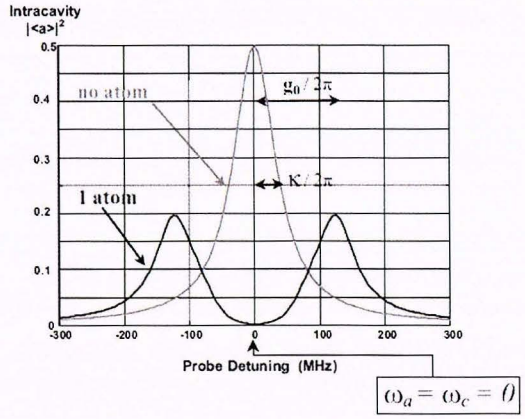

Figure 1.3: Vacuum-Rabi Splitting: An empty cavity transmission peak splits into two equally detuned peaks when an atom is strongly coupled to its electromagnetic field [7].

a single peak into a two-peak structure. With single atoms and photons, these peaks are detuned from the original peak by frequencies $\Delta_{\pm} = \pm g_0$, which correspond to $E_{\pm 1}$, the energy eigenvalues of $|\pm\rangle_1$.

The rate of coherent atom-field coupling (g_0) can be written as

$$g_0 = d \cdot E = d\sqrt{\frac{\hbar\omega}{2\epsilon_0 V_m}} \tag{1.5}$$

where d is the atomic dipole, ω is the resonant atomic transition frequency, V_m is the mode volume of the cavity, and $2g_0$ is the single photon Rabi frequency. From the strong coupling criterion $g_0 \gg (\kappa, \gamma, T^{-1})$, it is clear that the mode volume must be minimized in order to maximize g_0. This can be accomplished by using short cavity lengths ($l \sim 10^{-5}$ m) and mirrors with a steep radius of curvature ($r = 10$ cm). Minimizing κ is achieved by using superpolished low-loss mirrors ($\mathcal{F} \approx 4.8 \times 10^5$ at 852 nm), and maximizing T is achieved by employing laser cooling and trapping techniques.

1.1.2 Experiments in Cavity QED

The first cavity QED experiments in the regime of strong coupling at Caltech utilized atomic cesium beam transits through the optical cavity [8, 9]. The vacuum-Rabi splitting was obvserved by averaging over the atomic flux through the cavity and measuring the transmission spectrum of a tuneable weak probe beam about the cesium ($6S_{1/2}, F = 4, m_F = 4 \rightarrow 6P_{3/2}, F' = 5', m'_F = 5$) transition. The single atom vacuum-Rabi splitting was observed by setting the average intracavity atom number of the atomic beam to $\overline{N} = 1$ atom.

Combining cold atoms with cavity QED has allowed experiments to enter a new regime. By sub-Doppler cooling and then releasing a cloud of cesium atoms in a magneto-optic trap (MOT) a few millimeters above the cavity (see Figure 1.4a), the kinetic energy of the transit atoms was greatly reduced. It became possible to observe in real time the trajectories and transit durations of single atoms [10], as only one or two atoms crossed the standing-wave node of the cavity for each MOT drop.

There is also an interaction between cold atoms and the probe beam. An attractive pseudopotential is formed inside the cavity when the kinetic energy K of the transiting cesium atoms is less than $\hbar g_0$, the maximum of the atom-field coupling energy [5]. This characteristic has been exploited to create an atom-cavity microscope, in which the trajectory of a single atom is reconstructed from the probe beam transmission via an inversion algorithm (see Figure 1.4b) [11].

Additional experiments employing more elaborate trapping schemes have been carried out in the Kimble group, such as the creation of a one-atom laser [12], deterministic generation of single photons [13], and the mapping of the vacuum-Rabi spectrum for one-and-the-same atom [14].

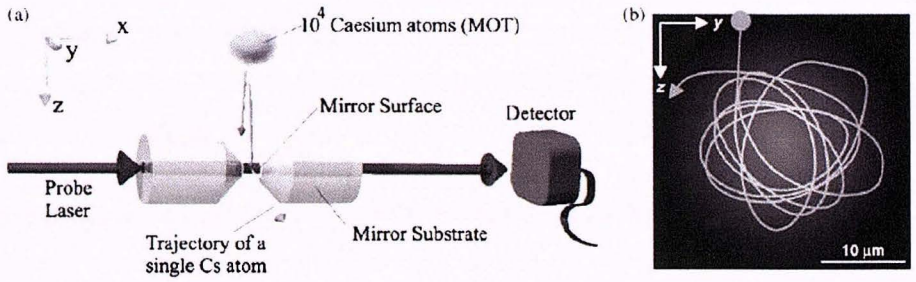

Figure 1.4: Schematic of the atom-cavity microscope: (a) Cesium atoms are laser cooled in a magneto-optic trap (MOT) before they are released just above the cavity. (b) The trajectory of a single atom's transit through the cavity can be reconstructed from the weak probe beam transmission [11].

1.2 A New Cavity

The decision was made in 2004 to replace one of our group's the optical cavities. For the remainder of this thesis I will refer to this cavity as the "lab 1 cavity" due to its physical location in Lab 1. Since the decision was made, efforts have been underway to improve and upgrade almost all components of the cavity and vacuum system. In particular, it was deemed necessary to upgrade the cavity's vibration isolation system. This became the focus of my thesis.

1.2.1 Motivation and Experimental Goals

The motivation for replacing the lab 1 cavity can be summarized in five main points.

1. Another working cavity would afford the opportunity for entanglement of atomic states between cavities, which has applications in quantum computation and communication [15].

2. The new cavity will be "single-sided." That is, one mirror will be more transmissive than the other, allowing light to escape primarily through the more transmissive one. We hope that this asymmetrical transmissiveness will improve our data collection and possibly bring about new physics to delve into, such as scalable photonic quantum computation as proposed by Duan and Kimble [16].

3. We would like to lower the background pressure in our vacuum chamber by a factor of 10. Collisions with background molecules contribute to our limit on storage time. With the current background pressure of 10^{-10} torr, we are able to store atoms via a FORT for about 3 seconds [17]. At 10^{-11} torr, we hope to achieve storage times of about 30 seconds in our new cavity. Extrapolating this factor of 10 is a bit shaky, as the limiting factor for storage right now could quite possibly be heating of the cesium atom by the lasers used to trap it [17, 18]. However, we hope to employ improved

cooling techniques so as to utilize the increased storage ability afforded by a lower background pressure.

4. In the past, attempts have been made to minimize stress-induced birefringent splitting in the cavity modes [7]. Now we will attempt to actively control the level of birefringence by squeezing the mirrors with piezoelectric transducers (PZTs).

5. Lastly, the lab 1 cavity will serve as a "backup cavity" in case the currently operational cavity in Lab 11 ever fails.

1.2.2 The Need for Mechanical Stability

The transmission of light through a Fabry-Perot cavity is given by [19]:

$$\frac{I_{trans}}{I_{inc}} = \frac{1}{1 + 4(\mathcal{F}/\pi)^2 \sin^2(kl)} \tag{1.6}$$

where $\mathcal{F}$ is the finesse of the cavity, $k = 2\pi/\lambda$ is the wavenumber of the incident light, and l is the length of the cavity. At resonance, the cavity length is equal to an integral number of half-wavelengths. Near resonance we can approximate this transmission by Taylor expanding the sine about zero, which yields the Lorentzian

$$\frac{I_{trans}}{I_{inc}} = \frac{\kappa^2}{\kappa^2 + (\nu - \nu_0)^2} \tag{1.7}$$

where $2\kappa = FSR/\mathcal{F}$ is the full width at half max (FWHM) linewidth of the cavity, ν is the injected light frequency, and $\nu_0 = ck = c\pi n/l$ for $n \in \mathbb{Z}$ is the resonant frequency of the cavity. A small change in length δl about ν_0 gives rise to a corresponding change in resonant frequency

$$\delta\nu_0 = -\frac{c\pi n}{l_0^2}\delta l = -\frac{\delta l}{l_0}\nu_0 \tag{1.8}$$

This equality can be used to express the transmission in terms of length:

$$\frac{I_{trans}}{I_{inc}} = \frac{1}{1 + (\delta\nu_0/\kappa)^2} = \frac{1}{1 + (\frac{\delta l}{\kappa l/\nu_0})^2} \tag{1.9}$$

The cavity's linewidth, expressed as a length, can be deduced from the squared term in the denominator in equation 1.9:

$$\Delta l_\kappa = \kappa\frac{l_0}{\nu_0} = \kappa\frac{\delta l}{\delta\nu_0} = \frac{\lambda_0}{8\pi\mathcal{F}} \tag{1.10}$$

The standard length stability requirement for our cavity QED experiments is 1/10 of a linewidth [20]. As described in Section 1.1.1, strong coupling requires ultra-high finesse cavities with small linewidths. The lab 1 cavity has finesse $\mathcal{F} = 480,000$ at 852 nm, thus requiring a length stability of about 7×10^{-14} m.

To achieve this strict level of length stability, the cavity must be well isolated from all sources of vibration. After good vibration isolation is achieved, we can actively servo the

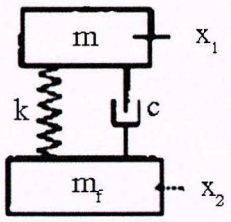

Figure 1.5: Schematic of a 1 degree of freedom vibration isolation stage: k is the linear stiffness of the elastic element, c is the damping coefficient, m and m_f are the masses of the isolated and foundation blocks respectively, and $m \ll m_f$.

length via piezos on which the mirrors are mounted. This thesis concerns the development of a new vibration isolation system (VIS) subject to three main constraints:

1. The components of the VIS must all be bakeable to upwards of 250° C. Previous VISs employed Viton, a fluoroelasotomer which is bakeable only to 200° C before decomposition [21]. A common technique to lower the achievable background pressure in an ultra high vacuum (UHV) chamber is to bake it at a high temperature, thereby expelling adsorbed gases at an accelerated rate in a process known as outgassing. This leads directly to the next contraint.

2. The components must all have low rates of inherent outgassing. Non-metal materials such as common elastomers and polymers typically have high outgassing rates which limit achievable levels of vacuum [22]. These materials must be avoided.

3. The VIS can utilize no permanent magnetic fields. We are interested in performing Raman sideband cooling, which requires a vanishing magnetic field, and thus there can be no stray magnetic fields present during the experiment.

1.3 Vibration Isolation

Seismic and acoustic vibration isolation is essential to many areas of modern experimental physics. In the atomic force microscopy (AFM) and scanning tunelling microscopy (STM) communities, effective vibration isolation plays a critical role in achieving satisfactory resolution [23]. The sensitivity of ground-based gravitational wave interferometers (GWIs) is greatly limited by low frequency seismic noise, so much research has been done to develop efficacious isolation systems for these experiments as well [24, 25, 26].

1.3.1 A Simple Model

Mechanical oscillators, which attenuate perturbations above their resonant frequency, serve as the fundamental building block for most VISs. Figure 1.5 shows a simple one degree of freedom schematic for a vibration isolation stage. We can characterize the isolation stage by its transfer function, given as a function of frequency [27]:

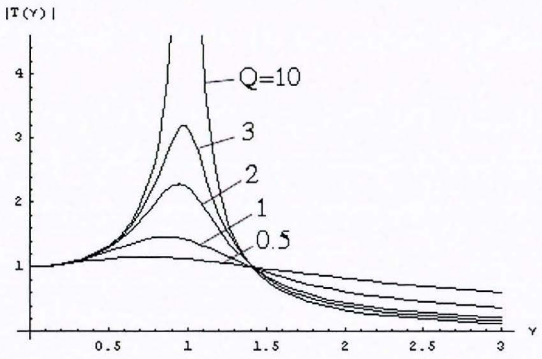

Figure 1.6: The transfer function of the system in Fig. 1.5, for $\nu_0 = 1$ and several values of Q.

$$|T(\nu)| = \frac{|x_1|}{|x_2|} = \sqrt{\frac{\nu_0^4 + \nu^2\nu_0^2/Q^2}{(\nu_0^2 - \nu^2)^2 + \nu^2\nu_0^2/Q^2}} \tag{1.11}$$

where $\nu_0 = \sqrt{k/\mu}$ is the resonant frequency of the system (with $\mu = mm_f/(m + m_f) \simeq m$ being the reduced mass), and $Q = \sqrt{k\mu}/c$ is the quality factor of the resonator. This transfer function exhibits a falloff above for frequencies above resonance which is approximately proportional to $1/\nu^2$ for frequencies in the range $\sqrt{2}\nu_0 < \nu < Q\nu_0$ and approximately proportional to $1/\nu$ for frequencies higher than $Q\nu_0$.

Figure 1.6 depicts $|T(\nu)|$ for $\nu_0 = 1$ and various values of Q. As can be seen from this plot, noise suppression for frequencies above the resonant frequency of the system can be maximized by minimizing ν_0. However, a there is an inherent tradeoff involved in choosing the quality factor of the oscillator: the falloff of the transfer function after the resonant frequency is steeper for higher Q values, but perturbations close to the resonant frequency will be amplified proportionally to Q. Thus, unless active damping is employed, a high-Q VIS will be ineffective in the vicinity of ν_0.

1.3.2 Common Vibration Isolation Systems

By stacking multiple isolation stages on top of each other, even better suppression can be achieved [28]. It is a common practice in many areas of physics to employ optical tables floating on pneumatic legs for vibration isolation. Such systems typically exhibit a resonant frequency around 2 Hz and excellent attenuation of seismic noise above this frequency. However, many experiments require even greater levels of noise suppression, necessitating additional isolation stages on top of the table.

In the AFM/STM communities, an efficient method of vibration isolation often used invovles suspending the microscope with springs [23]. When a single stage system does not suffice, a two-stage suspension spring system can be employed. A mathematical treatment of a two-stage isolator can be found in Section 4.1.1. The suppression of high frequency noise

for such a system with no viscous damping is excellent; however, the natural frequency resonances can be quite large. These resonances can be suppressed with damping, but at the cost of less high frequency suppression.

When experiments are not susceptible to magnetic fields, eddy-current damping is often utilized to meet these needs. A viscous force is introduced when a conductor has a velocity relative to a magnet. Thus, by establishing a magnetic field on a conducting suspension spring payload, the resonances can be damped by an amount related to the magnetic field strength.

Another drawback to a suspension spring VIS is its large size. A smaller system which is widely used comprises stacked metal plates separated by elastomers, which serve as the elastic element with intrinsic damping. The main drawback to this design is that it only provides effective isolation for relatively high frequencies [29]. Additionally, the stiffness of elastomers is highly nonlinear under load, making theoretical predictions difficult [23]. However, when combined with pneumatic tables, adequate vibration isolation can be achieved [23].

Chapter 2

Vibration Isolation Designs

This chapter discusses the previous VIS for the lab 1 cavity as well as two new designs proposed to improve both noise suppression and vacuum compatibility. All systems fit inside a cylidrical ultra high vacuum chamber (pictured in Figure 3.2) with a 4.3" diameter. This vacuum chamber is mounted on a large optical table with pneumatic legs. All mount contacts are separated by an elastomer, which provides further isolation between the chamber and the table.

2.1 The Previous System

Figure 2.1 shows the isolation system previously used for the lab 1 cavity. The large copper block serves as a base and is supported by axially loaded RTV (a silicone rubber) and Viton (a fluoroelastomer). Its shape is designed to maximize weight, thereby maximizing the compression of the rubber pieces and lowering the natural frequency. Its shape is also constrained to fit inside a cylindrical vacuum chamber and allow passage of diagonal laser beams.

The copper baseplate sits on four small strips of RTV. It is designed so that its center of mass is below its resting contact point, thus creating a pendulum mode for horizontal isolation. Finally, the cavity mount on top is supported by four pieces of Viton. The main design criterion for this mirror mount is that diagonal laser beams have passage to the cavity, which is glued to its upper surface.

Viton and RTV were chosen as elastic elements because they posess relatively low outgassing rates under high vacuum. However, as stated before, they have low maximum baking temperatures (200°C). We would like to be able to bake our new vacuum chamber at 250°C or higher, which would not be possible for these materials. Additionally, it would be best to minimize the amount of elastomers in the VIS, or to avoid the use of elastomers entirely to minimize outgassing.

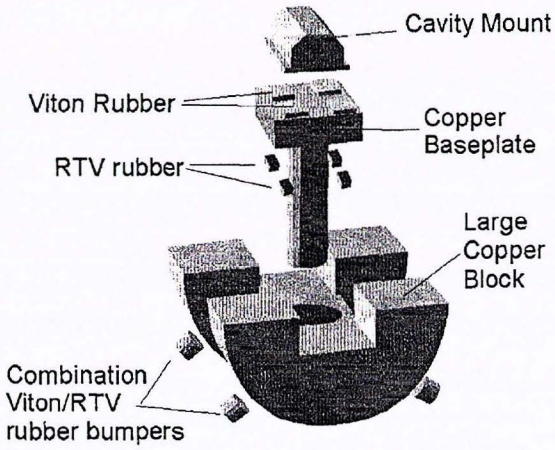

Figure 2.1: The previous VIS comprised three copper pieces, separated by a combination of Viton and RTV.

2.2 New Design: Kalrez

The first design of an improved VIS replaces all Viton and RTV pieces with Kalrez, a perfluoroelastomer. Kalrez, manufactured by DuPont Dow Elastomers, is bakeable to above 300°C without degradation. In fact, heat aging of Kalrez causes it to become more elastic as opposed to more embrittled like Viton [30]. Additionally, it has been shown to outgas at lower rates (but still same order of magnitude) than Viton over a wide temperature range, and at rates only 3-5 times higher than stainless steel at 300°C [31].

In addition to replacing the elastomeric elements with Kalrez, the VIS is modified by employing streamline loading of Kalrez. Examples of streamline loading include radially loaded spheres, cylinders, ellipsoids, and toruses (or toroidal sections, as in our case). By loading an elastomer radially as opposed to axially, compression is much more uniform. This modification in loading can produce lower natural frequencies and a 15-20% increase in damping [27]. A quantitative comparison of radial vs axial loading can be found in Section 4.1.

The hardness of an elastomer is rated on the Shore durometer scale. Kalrez, although comparable on the Shore scale to Viton, is much stiffer than RTV. Therefore, it is not unreasonable to expect marginal to no improvement in the overall performance of the Kalrez VIS. However, it is still worthwhile because of the higher baking temperature and lower outgassing rates the Kalrez VIS provides.

2.3 New Design: Blade Springs

Metal blade springs have been shown to produce effective filtering of seismic noise for GWI applications [26]. The use of geometric anti-spring (GAS) filters, as seen in Figure 2.2, has yielded vertical transfer functions with sub-hertz resonances [25].

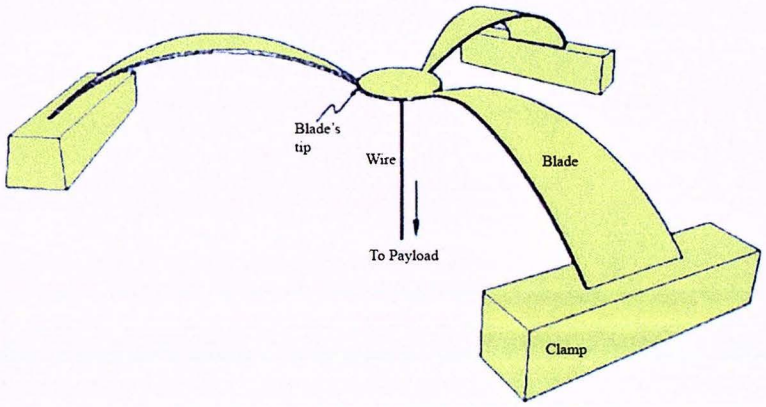

Figure 2.2: This is a three-blade GAS filter, similar to those used in GWIs such as LIGO, VIRGO, and TAMA [26].

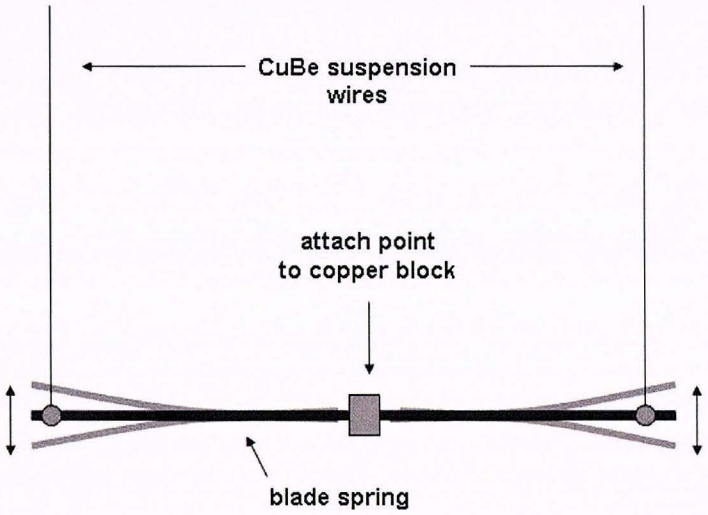

Figure 2.3: The two-blade mini-spring which will be used to suspend the cavity. Note the main differences between this spring and the one in Figure 2.2: the spring is attached directly to the payload, and it is suspended by wires which attach to the ends of the blade.

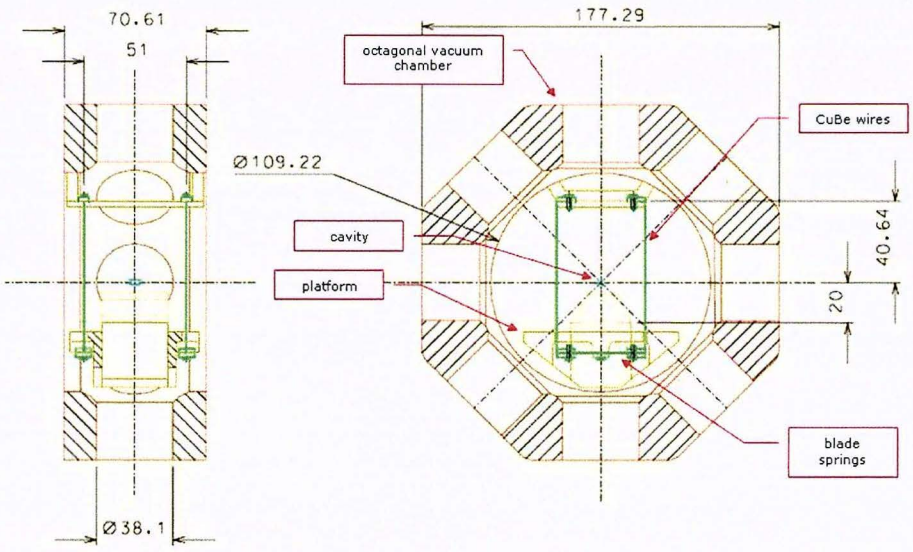

Figure 2.4: A side and axial schematic of the suspended platform and blade springs inside our vacuum chamber.

In collaboration with Riccardo DeSalvo (a LIGO scientist) and Gianni Gennaro (an Italian engineer), we have developed a miniaturized adapation of these blade springs to fit our isolation needs, as depicted in Figure 2.3. The design aims to achieve a 1 Hz vertical resonance from the blade spring, a 2 Hz pendulum resonance from the suspension wires, and a quality factor of about 100 [32]. Because the quality factor is so high, the transfer function should fall off steeply, but noise in the vicinity of 1 Hz will be greatly amplified. Therefore eddy-current damping must be incorporated, utilizing coils instead of permanent magnets.

A schematic of the entire suspension system inside the vacuum chamber is shown in Figure 2.4. Beryllium copper was chosen as the initial material for the suspension wires and blade springs because of its extremely non-magnetic properties. CuBe blade springs will relax under high baking temperatures, so Inconel blade springs will also be tested. Inconel springs retain strength to above 300° C [33].

Unfortunately, due to communication and fabrication delays, the timeline of the blade spring VIS has proven to be more extended than that of this thesis. The components for the system have been recently constructed, but additional preparation and testing (especially involving the use of MOT coils to implement eddy-current damping) is necessary before useful results can be presesnted.

Chapter 3

Analysis of VIS Performance

To analyze the noise suppression capabilites of the systems described in the previous chapter, two distinct methods are employed. First, a low-noise accelerometer is used to give an accurate reading of low frequency vibration levels with and without isolation elements.

While accelerometer readings give an accurate picture of vibrational noise, our experiments are ultimately sensitive to cavity length stability, which is indirectly related to vibration of the cavity mount. Because these vibrations cause the cavity length to change, the accelerometer results yield a good prediction of cavity stability. However, to get an explicit measure of cavity stability, a Pound-Drever-Hall lock on the cavity length is established, and variations in the closed-loop error signal of the lock are used to indicate cavity length noise.

3.1 Accelerometer Measurements

To get a detailed picture of low frequency vibrational noise being transmitted through the VIS, a high-sensitivity accelerometer (Wilcoxon model 797L) of approximately the same weight as the copper mirror mount ($\sim$ 100 g) was placed on the upper stage of the VIS. The accelerometer utilizes a piezoelectric transducer, which produces an AC signal on top of a bias DC voltage (Figure 3.1). This magnitude of the AC voltage is proportional to the acceleration of the piezoelectric element in a particular dimension (495 mV = 1 g).

Once the accelerometer is in place, the vacuum chamber is pumped down to $< 10^{-5}$ torr. Evacuating the chamber prevents acoustic coupling of noise inside the chamber, thereby restricting the accelerometer readings to noise which has penetrated the VIS.

After high-passing the output signal of the accelerometer at 0.16 Hz, the resulting signal is fed into a network analyzer which performs the Fast Fourier Transform (FFT). The accelerometer signal is quoted accurate to 5% between 0.6 Hz and 850 Hz, so data from the accelerometer will be restricted to this range. Calibrating this data yields a plot of acceleration spectral density ($g/\sqrt{Hz}$) vs. frequency (Hz). Displacement spectral density $D(\omega)$ is related to acceleration spectral density $A(\omega)$ by

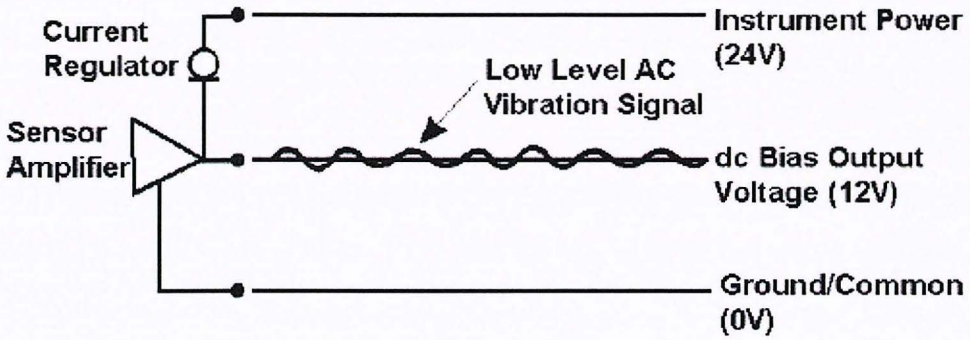

Figure 3.1: Electrical schematic of a piezoelectric accelerometer [34].

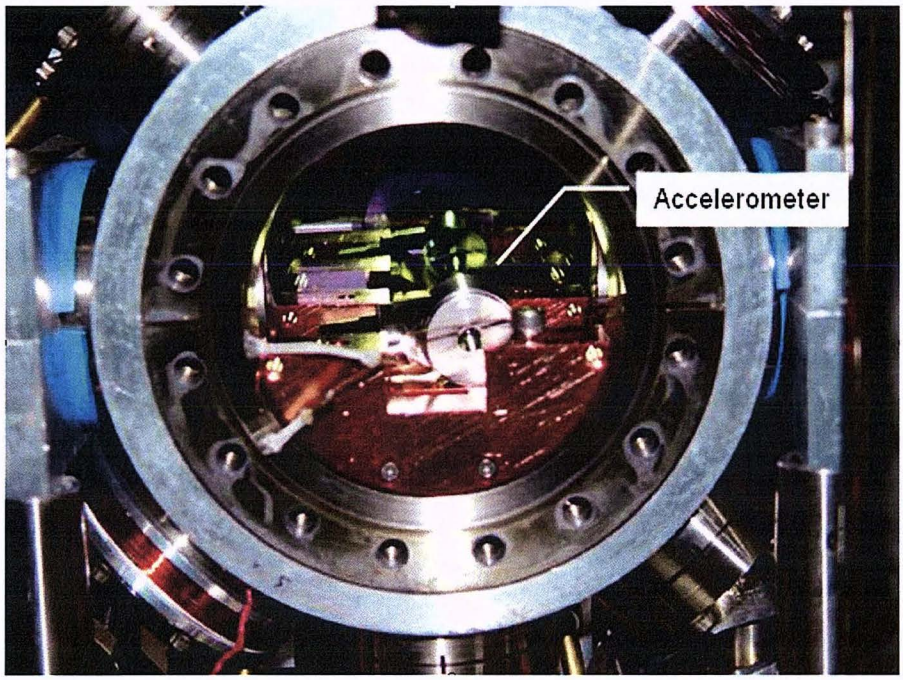

Figure 3.2: The accelerometer on the top stage of the VIS, inside the vacuum chamber.

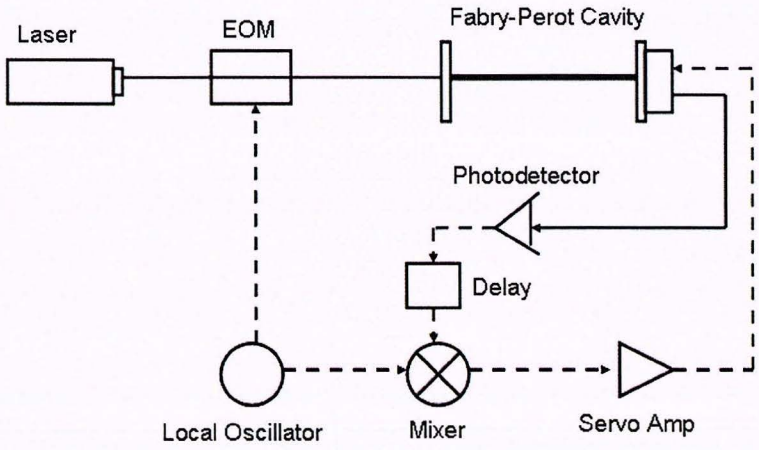

Figure 3.3: The experimental setup for Pound-Drever-Hall cavity length stabilization, looking at laser transmission. The solid lines represent the laser path, and the dashed lines represent electrical signal paths.

$$|D(\omega)| = \frac{|gA(\omega)|}{\omega^2} \tag{3.1}$$

The accelerometer has an inherent electrical noise which is about 0.5 $\mu g/\sqrt{Hz}$. For low frequencies ($\nu < 100$ Hz), vibrational noise is well above this noise floor. However, at higher frequencies, vibration is suppressed below this floor by both the Kalrez and Viton/RTV VIS.

Figure 3.2 is a photograph of the accelerometer in place before the chamber is evacuated. Transverse vibrations (on the axis of the cavity) contribute to cavity instability more than vertical vibrations, hence the accelerometer is posited transversely.

3.2 Pound-Drever-Hall Method

The Pound-Drever-Hall method is a powerful technique for laser frequency or cavity length stabilization. A detailed discussion of the technique as well as the experimental setup used for vibration analysis can be found in Appendix A. For the sake of brevity, this section will cover only the key points necessary to understand the method.

Figure 3.3 depicts the laser and signal paths involved in a typical Pound-Drever-Hall loop. The beam from a grating-stabilized diode laser is first phase modulated by an electro-optic modulator (EOM) before entering the Fabry-Perot cavity. The incident field may be written as

$$E_{inc} = E_0 e^{i(\omega t + \beta \sin \Omega t)} \tag{3.2}$$

where ω is the frequency of the carrier and Ω is the local oscillator (LO) frequency.

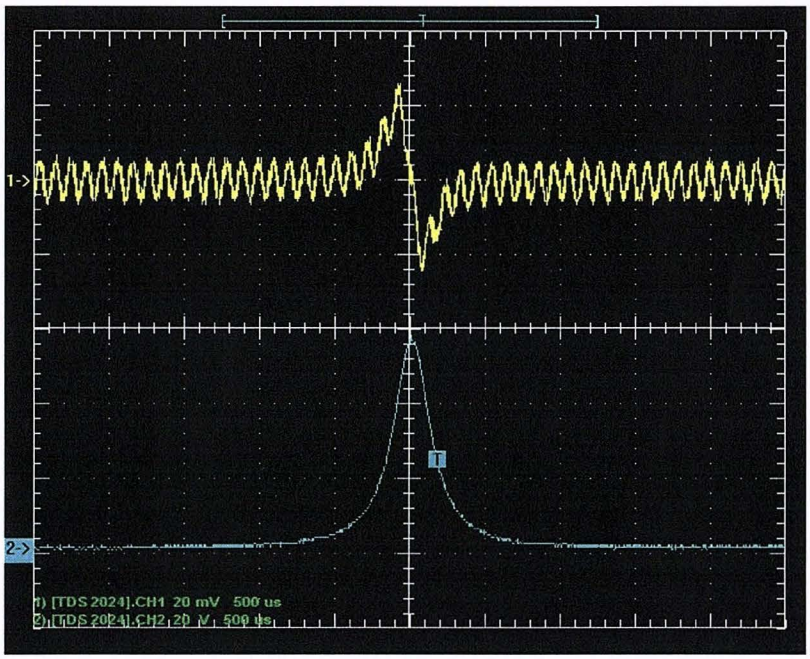

Figure 3.4: Cavity transmission is shown in blue, and Pound-Drever-Hall error signal is shown in yellow (with an abnormally large 60 Hz component present).

When the modulation frequency is small compared to the cavity linewidth, the field with instantaneous frequency $\omega + \beta\Omega\cos\Omega t$ has time to build up in the cavity. We may think of the incident field as containing a frequency dither which samples the slope of the cavity's transmission function, $T(\omega)$. In practice, the transmission of the cavity contains a component at frequency Ω whose amplitude is proportional to the magnitude of the slope of $|T(\omega)|^2$, and whose phase reflects the sign of the slope (0° below resonance and 180° above). The sign and slope are extracted by mixing the transmitted field with the LO to obtain the error signal, given by

$$\int_{-\infty}^{\infty} |E_{inc}|^2 e^{i\Omega t} dt \propto P_0 \frac{d|T(\omega)|^2}{d\omega}\Omega\beta \approx 2\sqrt{P_c P_s}\frac{d|T(\omega)|^2}{d\omega}\Omega \tag{3.3}$$

where P_0 is the power of the original beam, P_c is the power of the carrier beam, and P_s is the power of each sideband. Figure 3.4 is a oscilloscope trace of cavity transmission and error signal as the cavity length is swept with a triangle wave.

When close to resonance, the error signal is nearly linear with respect to cavity length noise. Thus, to lock the cavity length, the error signal is amplified and fed into an actuator (a PZT in our case) which controls the cavity length. A Fourier transform of this signal while the cavity is locked provides a good picture of cavity stability. A calibration and normalization technique for these FFTs is discussed in Appendix A. Because the control loop exhibits a unity-gain frequency around 10 Hz, FFT spectra are only accurate for higher frequency ranges. However, they are accurate over a much larger bandwidth than the accelerometer spectra.

Chapter 4

Experimental Results

4.1 Preliminary Tests: Radial vs. Axial Loading

To test the general vibration suppression properties of Kalrez and Viton, as well as the streamline loading predictions discussed in Section 2.2, a two stage vibration isolation stack, as shown in Figure 4.1, was assembled. The stack comprises two 2.5 kg stainless steel plates and two layers of elastomer. Three sets of accelerometer data were taken: one set with radially (streamline) loaded Kalrez, one set with axially loaded Viton, and one set with no elastic elements (so an experimental transfer function could be plotted).

The geometry of the elastomers was chosen such that all pieces were about the same size. Thus any major difference in vibration suppression is due to the difference in loading.

Each layer of elastomer was made up of three pieces. The Kalrez pieces were sections cut from a torus, with length $l \simeq 1$ cm and diameter $d = 0.32$ cm. The Viton pieces were axially loaded cylinders, with radius $r = 0.5$ cm and thickness $t \simeq 0.4$ cm.

4.1.1 Theoretical Model

The Kalrez sections were cut from a toroid, but they can be approximated as cylinders. The elastic spring constant of a radially loaded cylinder can be approximated by [27]

$$k_{rad} = E_0 l[1.88(\frac{x}{d})^{1/2} + 300(\frac{x}{d})^5] \tag{4.1}$$

where E_0 is Young's modulus, l is the length of the cylinder, d is its diameter, and x is the compression of the cylinder under load. Young's modulus is directly related to the Shore A durometer rating for an elastomer [35]. The Shore A rating for both Kalrez and Viton is 75, corresponding to $E_0 \simeq 9.2 \times 10^6 N/m^2$. For $x/d \simeq 0.1$ (an approximation for the setup described), the spring constant of each Kalrez piece is $k_K = 5.50 \times 10^4$ N/m.

An axially loaded cylinder of radius r and thickness t has an elastic spring constant [27]

$$k_{ax} \cong E_0(1 + \beta S^2) \tag{4.2}$$

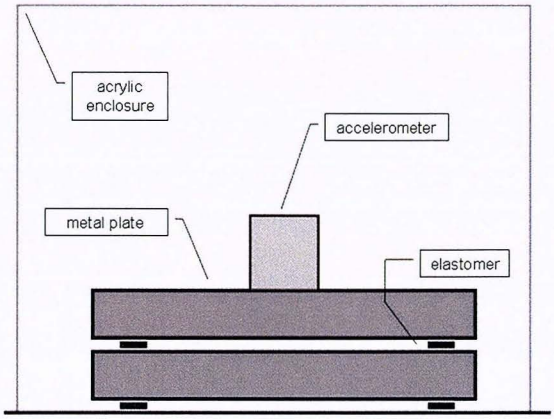

Figure 4.1: As a preliminary test, a two stage vibration stack was constructed as shown. Accelerometer readings were taken for radially loaded Kalrez, axially loaded Viton, and no elastomeric elements.

where $\beta \cong 1.04$ for Viton, and $S = r/2t$. Thus the spring constant for each Viton piece is $k_V = 2.35 \times 10^6$ N/m.

The transfer function for an undamped two-stage isolator with equal masses (m) and spring constants (k) is given by

$$T(\omega) = \frac{1}{\frac{n_1^2}{n_2^2}(\frac{\omega}{n_1})^4 - (1 + 2\frac{n_1^2}{n_2^2})(\frac{\omega}{n_1})^2 + 1} \tag{4.3}$$

where $n_1 = \sqrt{2k/m}$ and $n_2 = \sqrt{k/2m}$. The magnitude of this undamped transfer function, for both radially loaded Kalrez and axially loaded Viton, is shown in Figure 4.2a. The graph shows lower resonance frequencies (and ergo better high frequency suppression) for Kalrez. In reality, elastomers are damping materials, and thus one would not expect to see such large resonance peaks as this transfer function produces.

4.1.2 Accelerometer Results

An accelerometer was firmly secured to the top of the upper plate with a mounting screw, and the entire setup was enclosed in an acrylic box, which isolated the system from acoustic noise.

Because Kalrez and Viton have such a high intrinsic damping constant, the resonances in Figure 4.2b are well damped and difficult to pick out. Nevertheless, the theoretical and experimental curves are in fairly good agreeance.

We can define the cutoff frequency ν_c to be the point at which vibration suppression effectively begins (that is, the point where $|T(\nu)|$ falls below 0). Because the resonances are damped, the cutoff frequency is a more practical way of characterizing the isolators than the normal mode frequencies. As can be seen in Figure 4.2b, $\nu_c \approx 195$ Hz for the Viton configuration, and $\nu_c \approx 165$ Hz for the Kalrez configuration, a decrease of about 15%.

This decrease, although smaller than that for the undamped case, is in agreement with the theoretical predictions of streamline loading.

4.2 Testing the Isolation Systems

4.2.1 Model

To simplify calculations, the vibration isolation systems discussed in Chapter 2 can be roughly approximated as two-stage systems, grouping the copper baseplate and the mirror mount into one stage (since the mass of the mirror mount is small compared to the mass of the copper baseplate). Figure 4.3 is a plot of the undamped two-stage transfer function (Equation 4.3) of both VISs. Despite the advantage of streamline loading, the Kalrez VIS shows higher resonances than the Viton/RTV VIS. This is because RTV is much more elastic than Kalrez and Viton ($E_0 \approx 9 \times 10^5$ N/m).

4.2.2 Accelerometer Measurements

Figure 4.4 shows accelerometer spectra of the Viton/RTV and Kalrez systems, as well as a spectrum without elastic damping elements (No VIS). The Viton and Kalrez spectra fall below the noise floor ($\sim 0.5\ \mu g/\sqrt{Hz}$) of the accelerometer above 100 Hz. It is difficult to distinguish cutoff frequencies because the noise floor is relatively high, but they both appear to be between 70 Hz and 200 Hz.

In agreement with the theoretical model, the Viton/RTV system exhibits a large (factor of 10) resonance amplification between 20 Hz and 40 Hz, as can be seen clearly in 4.4a. Such an amplification corresponds to a quality factor $Q \approx 10$, which is larger than any Kalrez resonance quality factors apparent in the graphs. The Kalrez spectrum follows the no-VIS spectrum fairly well below 100 Hz, indicating a low quality factor. As discussed in Section 1.3, high-Q oscillators exhibit lower susceptibility above resonance than low-Q oscillators. So although Kalrez outperforms Viton/RTV in the low frequency range, it will be up to the Pound-Drever-Hall measurements to determine whether the high frequency suppression difference is appreciable.

4.2.3 Pound-Drever-Hall Measurements

Figure 4.5 shows the error signal spectra (cavity length density vs. frequency) produced by the different isolation systems. These spectra are calibrated and normalized using a method discussed in Appendix A. The substructure of error signal spectra under 100 Hz exhibited a variability of ~ 5 dB. However, the general falloff of the signal could be repeatably measured. Thus the most informative frequency spans are from 0 Hz to 400 Hz, which is right above where the VIS signals reach the noise floor.

With the exception of a few low frequency ($\nu < 100$ Hz) peaks, the Kalrez VIS provides better suppression than the Viton/RTV VIS below 400 Hz with the optical table not floated (Figure 4.5a). At this point the both isolation systems suppress noise below the noise floor of

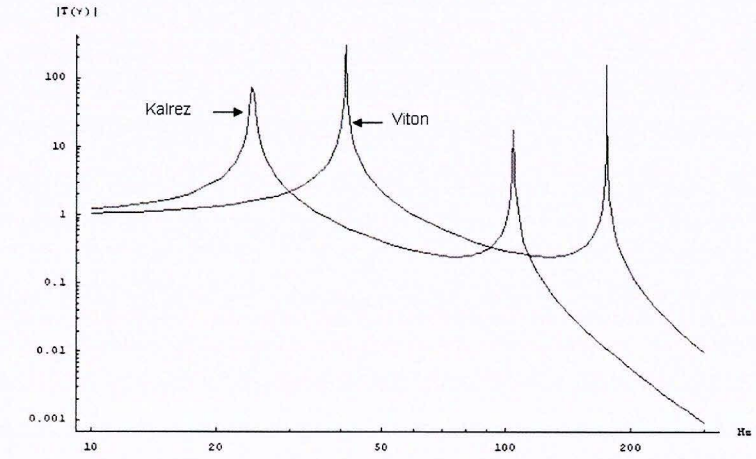

(a)

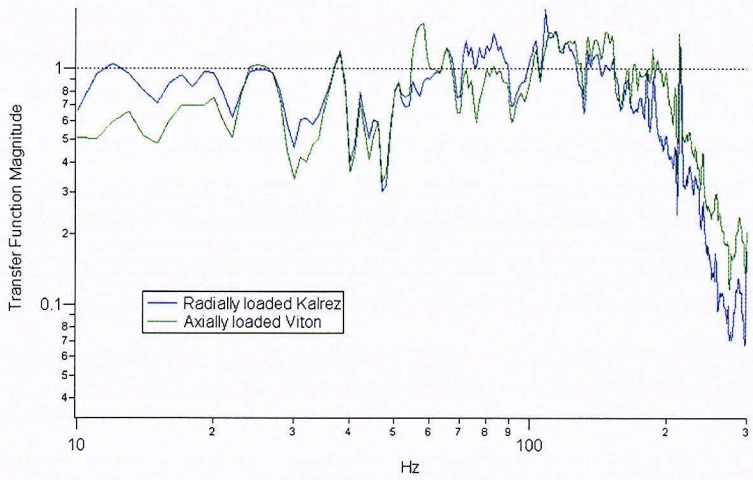

(b)

Figure 4.2: Theoretical (a) and experimental (b) transfer functions of the system shown in Figure 4.1, for radially loaded Kalrez and axially loaded Viton. The lower spring constant produced by radial loading leads to lower resonant frequencies.

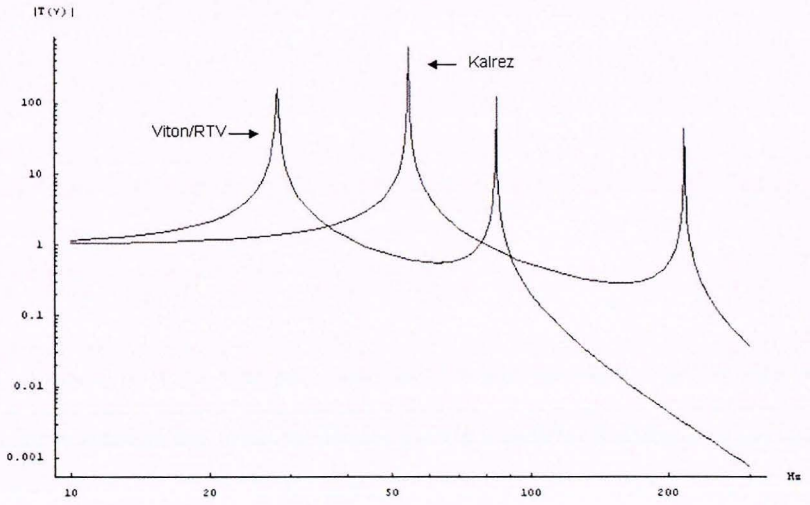

Figure 4.3: Undamped transfer functions of the Kalrez and Viton/RTV VISs, approximating them as two-stage systems.

our detection method ($\sim 10^{-15}\ m/\sqrt{Hz}$). The Kalrez VIS has a cutoff frequency $\nu_c \approx 170$ Hz, which is 15% lower than that for the Viton/RTV VIS ($\nu_c \approx 200$ Hz). Above 400 Hz, the error signals for both VISs fall to the noise floor, whereas the error signal for no VIS still shows structure. Figure 4.6 is a high frequency error signal FFT.

When cavity QED experiments are performed, the optical table supporting the vacuum chamber, lasers, and optics is floated on pneumatic legs to provide maximum seismic isolation. Figure 4.5b compares the error signal spectra of the two VISs when the table is floated. The cavity length stability afforded by the two systems is nearly identical in this situation.

In addition to the Kalrez VIS heretofore described, a variant VIS, which used 1/16" diameter Kalrez pieces, was tested. Figure 4.7 shows the resulting error signal spectra. The spectra cross between 150 Hz and 200 Hz, after which the original Kalrez VIS (large pieces) performs better.

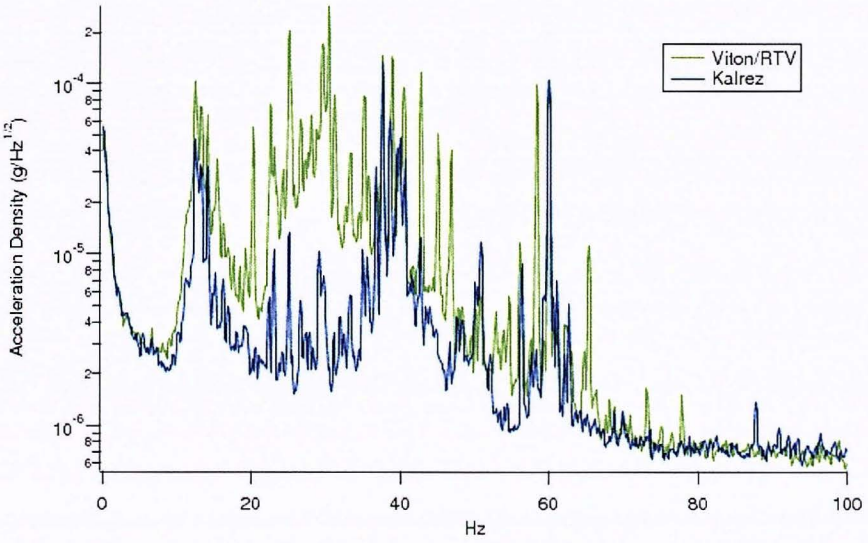

(a)

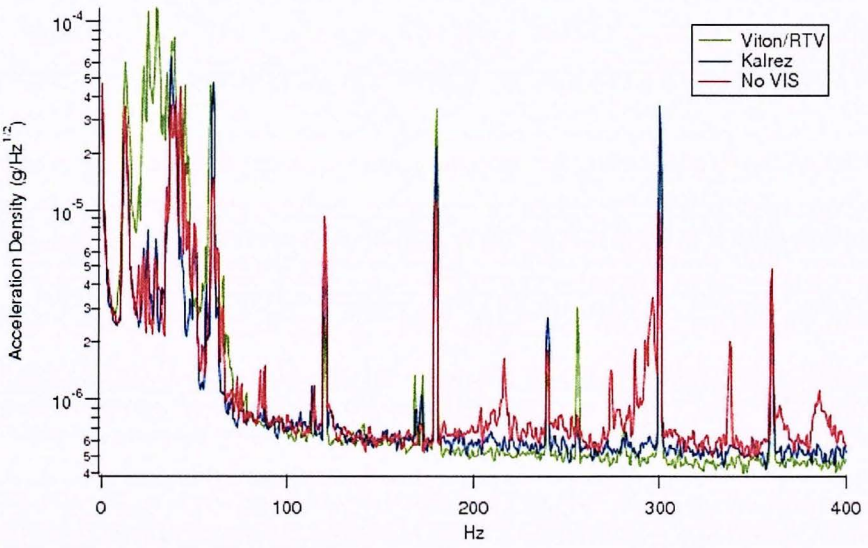

(b)

Figure 4.4: (a) Accelerometer spectra to 100 Hz of Viton/RTV VIS and Kalrez VIS. The RTV exhibits a large amplification of noise between 20 Hz and 40 Hz. The Kalrez transfer function in this range is essentially flat. (b) Accelerometer spectra to 400 Hz comparing VIS with Viton/RTV, Kalrez, and no elastic elements.

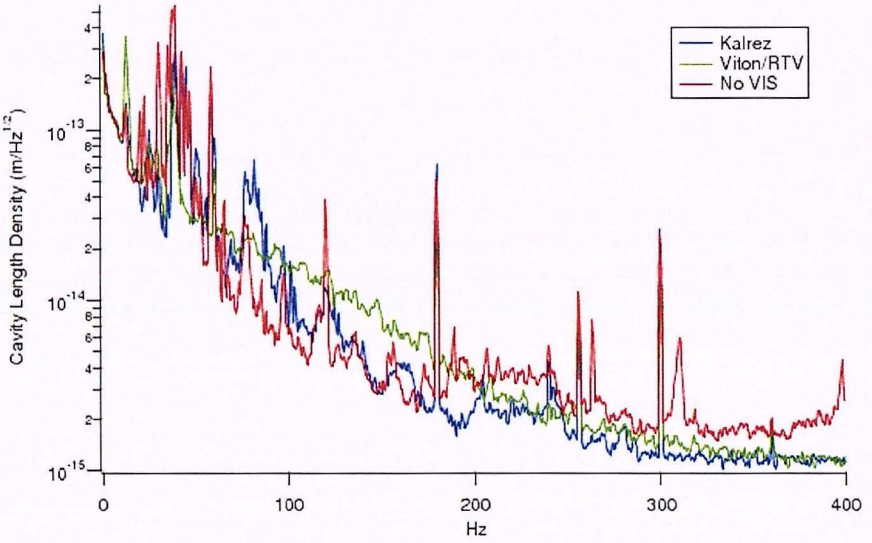

(a)

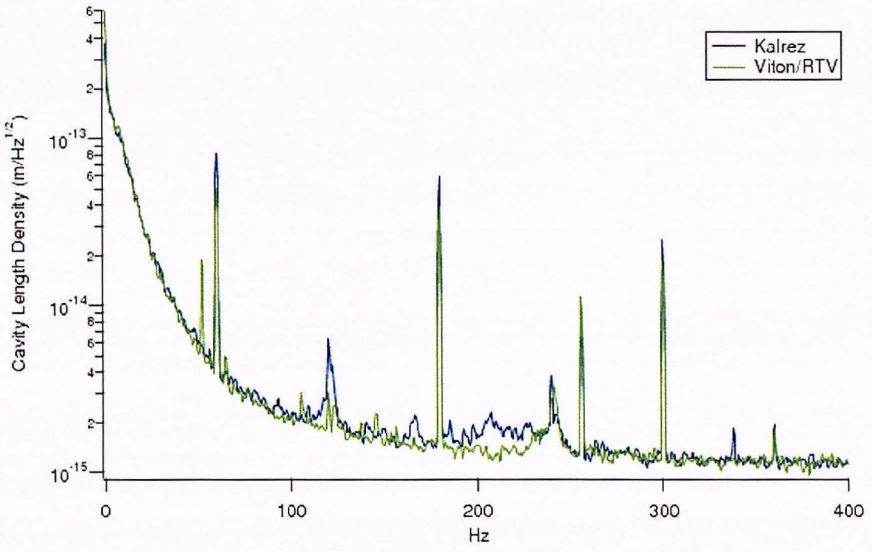

(b)

Figure 4.5: (a) Error signal spectra to 400 Hz of Viton/RTV VIS and Kalrez VIS, as well as no VIS. (b) Error signal spectra to 400 Hz with the optical table floated.

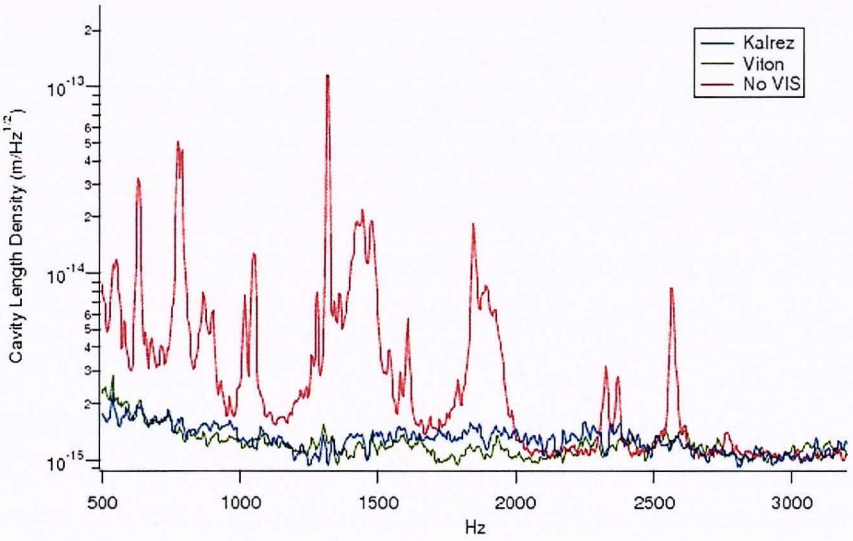

Figure 4.6: Error signal spectra of the Kalrez VIS and Viton/RTV VIS show suppression of vibrations below the noise floor.

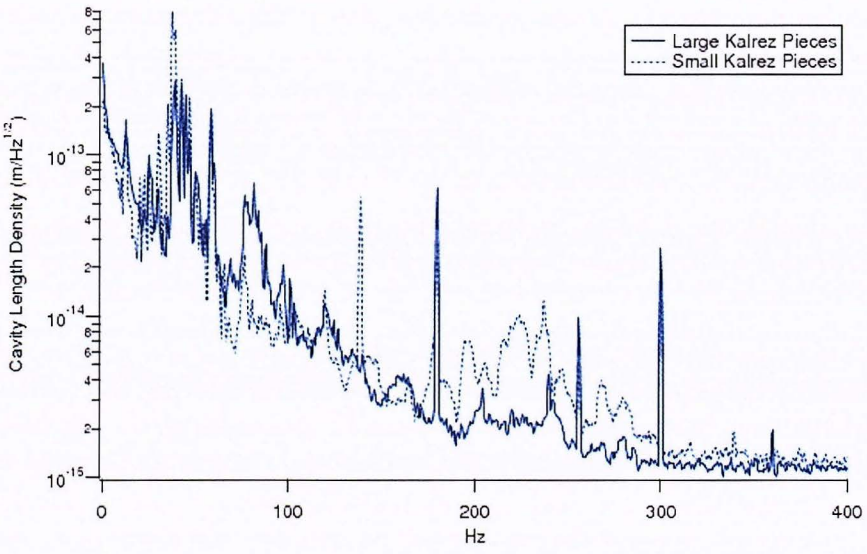

Figure 4.7: Error signal spectra from a Kalrez VIS using large (1/8" diameter) pieces and small (1/16" diameter) pieces.

4.3 Discussion of Results

A theoretical model for a two-stage isolator with radially/axially loaded elastic elements was presented and tested in Section 4.1.1. This model was subsequently applied to the Kalrez VIS and the Viton/RTV VIS in Section 4.2. VIS effectiveness, as well as the predictions made by this model, were tested with an accelerometer and with a Pound-Drever-Hall cavity lock.

The mechanism for how vibrational noise couples into cavity length noise is not entirely straightforward. Accelerometer spectra are good indicators of cavity stability, but there is no concrete relation between vibration spectral density and cavity length spectral density. The accelerometer spectra and the error signal spectra show approximately the same cutoff frequencies (although exact frequencies are difficult to ascertain in the accelerometer spectra).

The undamped theoretical model is also useful tool for making stability predictions. A large $\sim$ 30 Hz resonance for Viton/RTV was seen in the transfer function and both spectra. The model also predicted a $\sim$ 220 Hz resonance for Kalrez, which is supported by the error signal noise seen in this vicinity.

As described in Section 1.2.2, cavity length stability must be achieved to $< 10^{-13}$ m. The spectra in Figure 4.5b (with the optical table floated) indicate that this stability requirement is achieved above 20 Hz by both the Kalrez VIS and the Viton/RTV VIS (which was previously known to be sufficient). Figure 4.5a shows that this requirement is met for frequencies above 60 Hz, even without floating the table. Figure 4.6 indicates that the requirement is met above 400 Hz with no internal VIS nor with the table floated.

Up to this point, we purposefully handicapped the lock so as to enable noise characterization between 0 Hz and 400 Hz. With a higher gain and higher bandwidth lock, the noise is actively suppressed in this frequency range, and the stability requirement is easily met. The Kalrez VIS meets all design criteria: it is bakeable upwards of 300°C, it has outgassing characteristics superior to Viton and RTV, and it provides sufficient (as good as the Viton/RTV VIS) cavity stability.

Appendix A

Detecting Mirror Movement

The Pound-Drever-Hall method is a powerful technique for frequency stabilizing a laser, or conversely, length stabilizing an optical cavity [36]. In the former case, deviations in a laser's frequency are inferred from the power of its reflection off (or similarly transmission through) a stable Fabry-Perot cavity. This "error signal" is processed and then fed back to an actuator which controls the laser frequency. In the latter case, the error signal is created by deviations in cavity length. This error signal is fed back to an actuator which controls the cavity length. When implemented in a closed loop fashion, a properly processed error signal may be used to lock the laser's frequency to the cavity resonance, or vice versa.

A.1 Quantitative Model

The basic layout for Pound-Drever-Hall cavity locking is depicted in Figure 3.3. To generate a desirable error signal, a monochromatic laser is first phase-modulated via an electro-optic modulator (EOM) at a frequency provided by the Local Oscillator (LO). This modulation effectively places frequency sidebands on the laser. The electric field of this beam can be written as

$$E_{inc} = E_0 e^{i(\omega t + \beta \sin \Omega t)} \approx E_0[J_0(\beta)e^{i\omega t} + J_1(\beta)(e^{i(\omega+\Omega)t} - e^{i(\omega-\Omega)t})] \tag{A.1}$$

where ω is the carrier frequency, Ω is the modulation frequency, and J_n are Bessel functions. Given a cavity with complex transmission coefficient $T(\omega)$, the transmitted beam can be written as

$$E_{trans} = E_0[T(\omega)J_0(\beta)e^{i\omega t} + J_1(\beta)(T(\omega+\Omega)e^{i(\omega+\Omega)t} - T(\omega-\Omega)e^{i(\omega-\Omega)t})]. \tag{A.2}$$

When modulating at low modulation frequencies ($\Omega \ll FSR/\mathcal{F}$), the transmitted power can then be approximated as

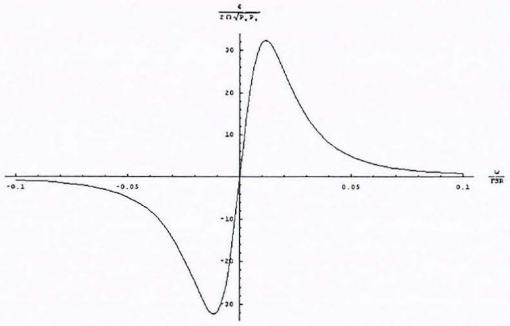

Figure A.1: The Pound-Drever-Hall error signal, $\epsilon/2\Omega\sqrt{P_c P_s}$ vs $\omega/\Delta\nu_{fsr}$ in the regime of slow modulation for a cavity with $\mathcal{F} \approx 300$.

$$P_{trans} = |E_{trans}|^2 \approx |E_0|^2 \frac{d|T(\omega)|^2}{d\omega} \Omega\beta \cos\Omega t + (constants) + (2\Omega\, terms) \tag{A.3}$$

where "2Ω terms" are terms that oscillate at frequency 2Ω. By appropriately phase shifting and mixing down the LO signal with this photodetector signal, the term oscillating at frequency Ω may be extracted. This is the Pound-Drever-Hall error signal:

$$\epsilon = P_0 \frac{d|T(\omega)|^2}{d\omega} \Omega\beta \approx 2\sqrt{P_c P_s} \frac{d|T(\omega)|^2}{d\omega} \Omega \tag{A.4}$$

where $P_0 = |E_0|^2$, $P_c = J_0^2(\beta)P_0$ is the power of the carrier, and $P_s = J_1^2(\beta)P_0$ is the power of the sidebands. Figure A.1 is a plot of this theoretical error signal for a cavity with finesse of 300.

Once the error signal has been generated, it is fed into a servo control box, where it is processed and transformed into a feedback signal. The feedback signal is then sent to an actuator which controls the length of the cavity.

Deviations in cavity length may be inferred from the error signal if the transfer functions of the control box and the actuator are known. Near the center of the resonance, the error signal is approximately linear. The error signal voltage V_e, piezo voltage V_p, and the cavity length l are thus related by

$$\frac{dl}{dV_e} = \frac{dl}{dV_p} \frac{dV_p}{dV_e} \tag{A.5}$$

The error signal on the lab 1 cavity has a peak-to-peak width of 4.46×10^{-11} m, coresponding to 13.5 volts on the piezo. Thus, for a 60 mV peak-to-peak error signal, $dl \simeq 7.41 \times 10^{-10} dV_e$.

A.2 The Control Loop and Unity Gain Frequency

The Pound-Drever-Hall technique requires a closed control loop to maintain cavity resonance. A generalized schematic of the control loop is shown in Figure A.2. Each component of the loop has a transfer function. These transfer functions must be taken into account

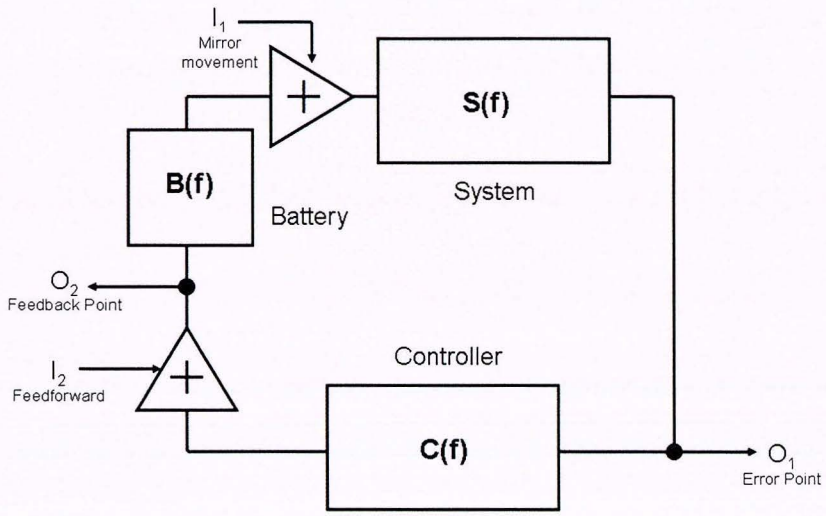

Figure A.2: Generalized schematic of the cavity lock control loop. S(f), C(f), and B(f) are the transfer functions of the system (laser, optics, detector, LO, mixer), control box, and battery box respectively.

when extracting the noise spectrum.

Such a loop produces negative feedback (suppressing length variations) at a gain above unity for frequencies below the unity gain frequency. Below this frequency, the mirror movement (I_1) is suppressed by the controller's gain [37]. Cavity length noise must be monitored at the feedback point (O_2). Above the unity gain frequency, however, the error point (O_1) is monitored to detect mirror movement.

The unity gain frequency occurs where $|C(f) \times S(f)| = 1$. If a disturbance such that $I_2 \gg I_1$ is fed forward to the loop, the signal at the feedback point can be approximated as

$$O_2 \approx I_2 + B(f)S(f)C(f)O_2 \tag{A.6}$$

Using a network analyzer, O_2/I_2 can be measured. The unity gain frequency is thus where the equality

$$|C(f) \times S(f)| = |\frac{1}{B(f)}[\frac{I_2}{O_2} - 1]| = 1 \tag{A.7}$$

holds true. The control loop for the lab 1 cavity initially had a unity gain frequency around 4 kHz. The unity gain frequency was reduced to about 10 Hz (depending on the exact gain settings of the lockbox) by adding a 0.16 Hz high-pass filter to the lock box output, thus allowing the error signal to be used for monitoring cavity length noise in the seismic range.

A.3 Noise Limits

There are two main noise sources which cavity length noise must contend with when analyzing the error signal. The first is shot noise, which arises due to the quantum nature of light. For a laser of power P and wavelength λ, the shot noise has a constant spectral density given by

$$\xi_{shot} = \sqrt{2\frac{hc}{\lambda}P} \tag{A.8}$$

where h is Planck's constant, c is the speed of light [36]. This noise can be divided by the slope of the error signal to yield the apparent length noise. In practice, however, the shot noise is affected by the adjustable gain of the photodetector, the RF amplifier, mixer, etc. In conjunction with other noise sources (primarily electrical noise, including the omnipresent line noise at 60 Hz and harmonies), the shot noise contributes to the overall noise floor of the control loop, which corresponds to about $10^{-15}\ m/\sqrt{Hz}$.

An additional source of noise affecting the error signal is the FM noise of the laser. This noise scales linearly with cavity length, so it can be minimized by utilizing very short cavities. The lab 1 cavity used for error signal measurements in this thesis has finesse $\mathcal{F} \approx 400$ at $\lambda = 935$ nm, and a length $l \approx 20\ \mu$m. Near resonance, a fractional change in length dl/l for a fixed laser frequency will appear the same as a fractional frequency change $d\omega/\omega$ for a fixed cavity length. Thus to disregard FM noise, we must have:

$$\frac{d\omega}{\omega} \ll \frac{dl}{l}$$

$$\Rightarrow d\omega \ll \frac{\omega}{l}dl \simeq 10^{19}dl \tag{A.9}$$

The linewidth of the grating-stabilized diode laser is less than 100 kHz. Thus FM noise does not affect the error signal on the same order as cavity noise until length deviations are approaching $10^{-15}\ m/\sqrt{Hz}$.

A.4 Normalization of Spectra

In order to lock the cavity, the error signal must be amplified at a gain which is inversely proportional to its slope. However, for different gain settings, the transfer function of the control loop is changed (the unity gain frequency of the loop is shifted), and the resulting error signal spectra appear remarkably different.

To remedy this discrepancy, a normalization scheme to account for differences in error signal size and gain settings was developed. After an error signal spectrum is taken, the feed-forward point of the loop (I_2 in Figure A.2) is injected with a swept sine signal from the network analyzer. If the swept sine signal is large compared to the vibration noise, but small enough that the closed loop error signal remains in the linear regime, then monitoring the error point O_1 as a function of swept sine frequency provides the closed loop transfer

function. The logarithmic difference in transfer functions between two different spectra can then be added to one spectrum, thereby normalizing the two.

Figure A.3 shows the results of this normalization scheme, comparing high and low gain FFTs and sine sweeps (with the same VIS).

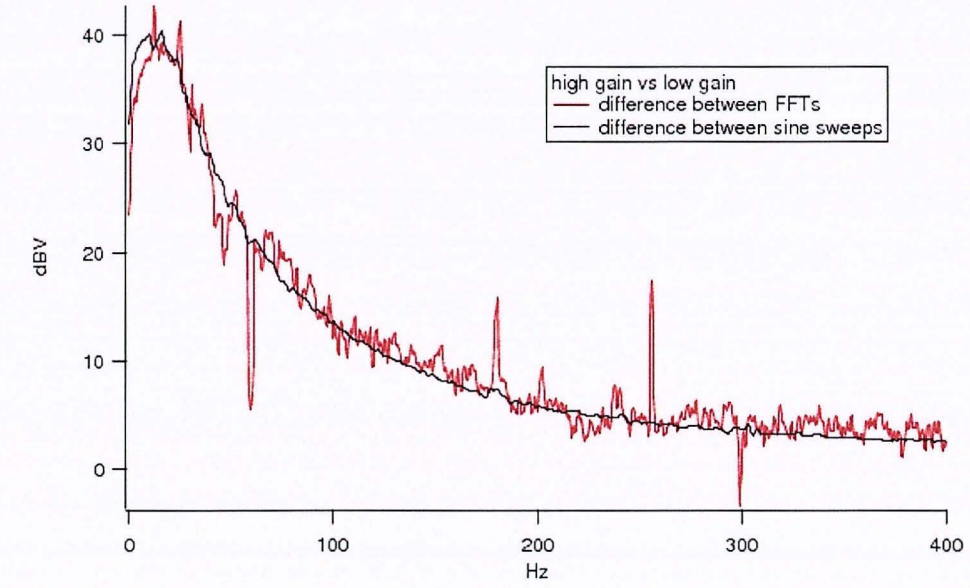

(a)

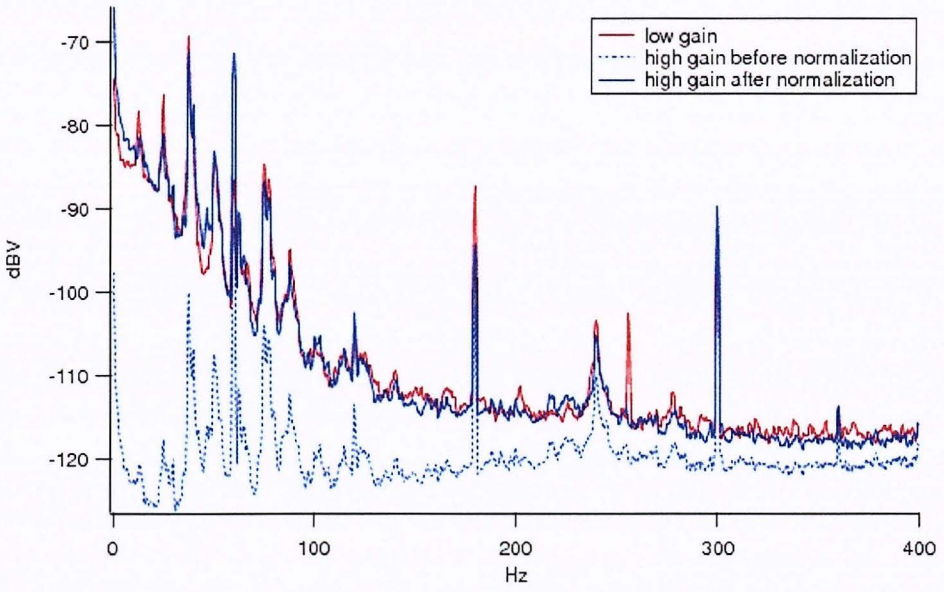

(b)

Figure A.3: (a) The difference between two error signal FFTs at different gain settings is compared to the difference between their closed loop transfer functions. (b) A high gain FFT is normalized to a low gain FFT.

Bibliography

[1] H. J. Kimble, "Strong interactions of single atoms and photons in cavity QED," *Physica Scripta* **T76**, p. 127, 1998.

[2] D. C. Ralph, C. T. Black, and M. Tinkham, "Gate-voltage studies of discrete electronic states in aluminum nanoparticles," *Phys. Rev. Lett.* **78**, p. 4087, 1997.

[3] D. Leibfried, R. Blatt, C. Monroe, and D. Wineland, "Quantum dynamics of single trapped ions," *Rev. Mod. Phys.* **75**, p. 281, 2003.

[4] C. J. Hood, M. S. Chapman, T. W. Lynn, and H. J. Kimble, "Real-time cavity QED with single atoms," *Phys. Rev. Lett.* **80**, p. 4157, 1998.

[5] R. Miller, T. E. Northup, K. M. Birnbaum, A. Boca, A. D. Boozer, and H. J. Kimble, "Trapped atoms in cavity QED: coupling quantized light and matter," *J. Phys. B: At. Mol. Opt. Phys.* **38**, pp. S551–S565, 2005.

[6] E. T. Jaynes and F. W. Cummings, "Comparison of quantum and semiclassical radiation theories with application to beam maser," *P. IEEE* **51**, p. 89, 1963.

[7] T. W. Lynn, *Measurement and control of individual quanta in cavity QED.* PhD thesis, California Institute of Technology, 2003.

[8] R. J. Thompson, G. Rempe, and H. J. Kimble, "Observation of normal-mode splitting for an atom in an optical cavity," *Phys. Rev. Lett.* **68**, p. 1132, 1992.

[9] G. Rempe, R. J. Thompson, R. J. Brecha, W. D. Lee, and H. J. Kimble, "Optical bistability and photon statistics in cavity quantum electrodynamics," *Phys. Rev. Lett.* **67**, p. 1727, 1991.

[10] H. Mabuchi, Q. A. Turchette, M. S. Chapman, and H. J. Kimble, "Real-time detection of individual atoms falling through a high-finesse optical cavity," *Opt. Lett.* **21**, p. 1393, 1996.

[11] C. J. Hood, T. W. Lynn, A. C. Doherty, A. S. Parkins, and H. J. Kimble, "The atom-cavity microscope: single atoms bound in orbit by single photons," *Science* **287**, p. 1457, 2000.

[12] J. McKeever, A. Boca, A. D. Boozer, J. R. Buck, and H. J. Kimble, "Experimental realization of a one-atom laser in the regime of strong coupling," *Nature* **425**, p. 268, 2003.

[13] J. McKeever, J. R. Buck, A. D. Boozer, and H. J. Kimble, "Determination of the number of atoms trapped in an optical cavity," *Phys. Rev. Lett.* **93**, p. 143601, 2004.

[14] A. Boca, R. Miller, K. M. Birnbaum, A. D. Boozer, J. McKeever, and H. J. Kimble, "Observation of the vacuum Rabi spectrum for one trapped atom," *Phys. Rev. Lett.* **93**, p. 233603, 2004.

[15] L.-M. Duan and H. J. Kimble, "Efficient engineering of multiatom entanglement through single-photon detection," *Phys. Rev. Lett.* **90**, p. 253601, 2003.

[16] L.-M. Duan and H. J. Kimble, "Scalable photonic quantum computation through cavity-assisted interactions," *Phys. Rev. Lett.* **92**, p. 127902, 2004.

[17] J. R. Buck Jr., *Cavity QED in microsphere and Fabry-Perot cavities.* PhD thesis, California Institute of Technology, 2003.

[18] J. McKeever, J. R. Buck, A. D. Boozer, A. Kuzmich, H.-C. Nägerl, D. M. Stamper-Kurn, and H. J. Kimble, "State-insensitive cooling and trapping of single atoms in an optical cavity," *Phys. Rev. Lett.* **90**, p. 133602, 2003.

[19] F. DeMartini and C. Monroe, eds., *Experimental Quantum Computation and Information*, IOS Press, 2002.

[20] C. J. Hood, *Real-time measurement and trapping of single atoms by single photons.* PhD thesis, California Institute of Technology, 2000.

[21] D. Coyne, "Viton spring seat vacuum bake qualification," ligo-t970168-00-d, HYTEC Inc., Los Alamos, NM, 1997.

[22] W. G. Perkins, "Permeation and outgassing of vacuum materials," *J. Vac. Sci. Technol.* **10**, p. 4, 1973.

[23] C. J. Chen, *Introduction to Scanning Tunneling Microscopy*, Oxford University Press, 1993.

[24] C. Wang, H. Tariq, R. DeSalvo, Y. Iida, S. Marka, Y. Nishi, V. Sannibale, and A. Takamori, "Constant force actuator for gravitational wave detector's seismic attenuation systems (SAS)," *Nucl. Instr. and Meth. A* **489**, p. 563, 2002.

[25] A. Takamori, M. Ando, A. Bertolini, G. Cella, R. DeSalvo, M. Fukushima, Y. Iida, F. Jacquier, S. Kawamura, S. Marka, Y. Nishi, K. Numata, V. Sannibale, K. Somiya, R. Takahashi, H. Tariq, K. Tsubono, J. Ugas, N. Viboud, H. Yamamoto, T. Yoda, and C. Wang, "Mirror suspension system for the TAMA SAS," *Class. Quantum Grav.* **19**, p. 1615, 2002.

[26] M. Mantovani, *Minimizing the Resonant Frequency of MGAS Springs for Seismic Attenuation System in Low Frequency Gravitational Wave Interferometers.* PhD thesis, Universita di Pisa, 2004.

[27] E. I. Rivin, *Passive Vibration Isolation*, ASME Press, 2003.

[28] J. Lawall and E. Kessler, "Design and evaluation of a simple ultralow vibration vacuum environment," *Rev. Sci. Instr.* **73**, p. 209, 2002.

[29] A. I. Oliva, M. Aguilar, and V. Sosa, "Low- and high-frequency vibration isolation for scanning probe microscopy," *Meas. Sci. Technol.* **9**, p. 383, 1998.

[30] J. G. Drobny, *Technology of Fluoropolymers*, CRC, 2000.

[31] M. F. Zabielski and P. R. Blaszuk, "Vacuum evaluation of a new perfluoroelastomer," *J. Vac. Sci. Technol.* **13**, p. 2, 1978.

[32] R. Passaquieti, "Re: vibration measurements." Email to S.T. Bannerman, aug 2005.

[33] S. C. Taylor, J. J. D. adn Patrick H. Dunlap, and B. M. Steinetz, "Evaluation of high temperature knitted spring tubes for structural seal applications," tech. rep., NASA, 2004.

[34] Wilcoxon Research, "Technical note 14: Trouble shooting industrial accelerometer installations."

[35] J. Daniel L. Hertz, "O-rings for low-pressure service," tech. rep., Seals Eastern, 1979.

[36] E. D. Black, "An introduction to Pound-Drever-Hall laser frequency stabilization," *Am. J. Phys.* **69**, p. 79, 2001.

[37] V. Leonhardt, *Displacement measurements on suspended mirrors for off-resonant thermal noise detection.* PhD thesis, Universitat Hannover, 2003.